CrystEngComm

PAPER

View Article Online
View Journal

Cite this: DOI: 10.1039/c8ce01351a

From light to heavy alkali metal tetraphosphonates (M = Li, Na, K, Rb, Cs): cation size-induced structural diversity and water-facilitated proton conductivity†

Inés R. Salcedo,[a] Rosario M. P. Colodrero,[b] Montse Bazaga-García,[a] Antonia Vasileiou,[c] Maria Papadaki,[c] Pascual Olivera-Pastor,[a] Antonia Infantes-Molina,[a] Enrique R. Losilla,[a] Gellert Mezei,*[d] Aurelio Cabeza*[a] and Konstantinos D. Demadis*[c]

Received 11th August 2018,
Accepted 16th September 2018

DOI: 10.1039/c8ce01351a

rsc.li/crystengcomm

A family of alkali metal-based frameworks containing the tetraphosphonate ligand hexamethylenediamine-*N*,*N*,*N*′,*N*′-*tetrakis*(methylenephosphonic acid), HDTMP, is reported. A cation size-induced structural diversity, from monodimensional solids (Li^+ and Na^+) through layered (K^+) to pillared-layered (Rb^+ and Cs^+) structures, was found. The proton conductivity properties of the Li compounds (hydrated and dehydrated) are reported and the influence of dehydration/rehydration processes in enhancing proton transfer processes is highlighted. Reversible changes in the dimensionality occurred upon full dehydration/rehydration with minor rearrangements in the framework, implying variations in the Li^+–ligand connectivity but preserving the tetracoordination of the metal ion. The reversibly dehydrated–rehydrated sample displayed the highest proton conductivity (5×10^{-3} S cm^{-1} at 80 °C and 95% RH), a behavior attributed to reversible formation/reformation of P–O(H)–Li bonds that, in turn, provoked changes in the acidity of acid groups and water mobility in the temperature range of impedance measurements.

1. Introduction

The field of metal phosphonate compounds has experienced constant growth during the last decades.[1] This is primarily due to the rich structural diversity of these hybrids and their potential applications,[2] including gas storage,[3–5] photoluminescence,[6,7] proton conductivity,[8–14] corrosion control[15–20] and metal ion absorption.[21,22] Phosphonic acids and their water-soluble salts find extensive use in several industrial and pharmaceutical applications, such as mineral

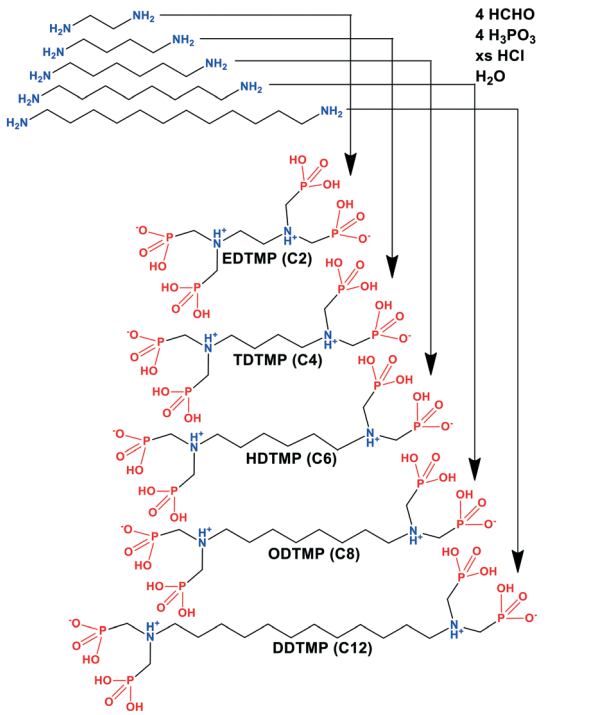

Scheme 1 Schematic structures of the tetraphosphonate family members in their zwitterionic form.

[a] *Departamento de Química Inorgánica, Universidad de Málaga, Campus Teatinos s/n, Málaga-29071, Spain. E-mail: aurelio@uma.es*
[b] *Faculty of Science & Engineering, University of Wolverhampton, Wulfruna Street, Wolverhampton WV1 1LY, UK*
[c] *Crystal Engineering, Growth and Design Laboratory, Department of Chemistry, University of Crete, Voutes Campus, Crete, GR-71003, Greece. E-mail: demadis@uoc.gr*
[d] *Department of Chemistry, Western Michigan University, Kalamazoo, Michigan 49008-5413, USA. E-mail: gellert.mezei@wmich.edu*

† Electronic supplementary information (ESI) available: CIF files for all **M-HDTMP** compounds (M = Li, Na, K, Rb, and Cs), Rietveld plot for **Li-HDTMP-0W**, powder XRD patterns, ATR-IR spectra, additional TGA traces, graphs relating coordination numbers and M–O bond distances with cation size, and impedance results. CCDC 1584815–1584820. For ESI and crystallographic data in CIF or other electronic format see DOI: 10.1039/c8ce01351a

scale inhibition,[23–25] dispersion,[26] scale dissolution,[27] osteoporosis treatment,[28–30] cancer treatment,[31] *etc.*

Among the plethora of phosphonic acid linkers/ligands, those possessing the amino-bis(methylenephosphonate) moiety are useful tools in crystal engineering and materials synthesis because they offer the possibility of structural systematics. More specifically, a whole family of tetraphosphonate linkers can be synthetically accessed *via* a Mannich-type (Irani–Moedritzer) reaction.[32–34] In principle, this reaction allows the clean transformation of a primary amine to an amino-bis(methylenephosphonic acid) moiety. Hence, an aliphatic primary amine yields a diphosphonic acid.[35] By using α,ω-diaminoalkanes the corresponding tetraphosphonic acids can be synthesized, as shown in Scheme 1. These tetraphosphonic acids are versatile building blocks that generate a variety of structures with different topologies, including closely packed three-dimensional[36–39] and pillared layered networks[40] and some hybrids with layered structures having the phosphonic groups situated within the layers.[41,42]

Regarding the linker HDTMP, a variety of structures ranging from 1D to 3D architectures have been reported.[40,43–48] Some representative examples of these materials are: CaHDTMP, which provided the first example of a breathing-like mechanism in metal phosphonates presenting a 2D topology,[42] La(HDTMP)·7H_2O, a 3D pillared open-framework ultramicroporous material with high proton conductivity and strong irreversible NO adsorption capacity,[45] and $[Ln_2(SO_4)_2(HDTMP)(H_2O)_4]\cdot 10H_2O$ (Ln = Eu^{3+}, Sm^{3+} and Gd^{3+}), a family of isotypical 3D MOFs obtained by a fast microwave-assisted methodology, which decreased considerably the reaction times for the synthesis.[49] Recently, the synthesis routes, structural diversity and properties (*e.g.*, photoluminescence, proton conductivity, ion-exchange and heterogeneous catalysis) exhibited by lanthanide tetraphosphonic-based metal–organic frameworks have been reviewed.[50]

In this paper, we report the synthesis and structural characterization of a family of alkali metal frameworks containing the ligand hexamethylenediamine-*N*,*N*,*N*′,*N*′-*tetrakis*-(methylenephosphonic acid), HDTMP. The proton conductivity properties of the lithium compounds are reported and the influence of the dehydration/rehydration processes in enhancing the proton transfer processes is highlighted.

2. Experimental section

2.1 Reagents and materials

The starting alkali metal salts and hydroxides were from commercial sources and used as received (LiOH·H_2O, KOH, and CsCl were from Riedel-de Haen, and NaOH and RbOH were from Sigma Aldrich). H_8DTMP (Dequest 2051) was from ThermPhos-Dequest, Belgium. Deionized (DI) water from a laboratory cation exchange column was used for all syntheses.

2.2 Synthesis of alkali metal-HDTMP compounds

All **M-HDTMP** compounds were prepared in a similar manner. As an example, we provide synthetic details for **Li-HDTMP**. A general observation is that all **M-HDTMP** products are water-soluble and do not crystallize out from pure aqueous solutions, as several M(II), M(III) or M(IV) phosphonates do. Hence, the use of organic co-solvents as precipitants is necessary.

Li-HDTMP-4W, $[Li_2(HDTMP)(H_2O)_4]$. Solid HDTMP acid (0.492 g, 1.000 mmol) is added to 20 mL of DI water under stirring. Separately, LiOH·H_2O (0.042 g, 1.000 mmol) is dissolved in 10 mL DI water. The latter solution is added to the first one dropwise, and the stirring continues until a clear colorless final solution is obtained in a glass test tube (2 cm diameter). The magnetic stirring bar is removed and 20 mL of EtOH is carefully layered on top of the aqueous layer with a Pasteur pipette, forming a H_2O/EtOH layer. The system is covered with Parafilm and left undisturbed for 2 weeks, after which large colorless needle-like crystals form. They are isolated by filtration, washed with EtOH and air-dried. Yield ~50%. Elemental analysis for $Li_2(P_4O_{12}N_2C_{10}H_{26})\cdot 4H_2O$ (MW = 576.16 g mol^{-1}). Calculated, %: C 20.85, H 5.95, N 4.86. Found, %: C 20.40, H 5.83, N 5.02.

Li-HDTMP-0W, $[Li_2(HDTMP)]$. Heating **Li-HDTMP-4W** at 200 °C for 2 h led to a new anhydrous crystalline phase (**Li-HDTMP-0W**), which rehydrated, slowly under ambient conditions and quickly at 80 °C and 95% relative humidity (RH).

Na-HDTMP, $[Na_2(HDTMP)(H_2O)_{6-8}]$. The quantities used were: solid HDTMP (0.984 g, 2.000 mmol) and NaOH (0.160 g, 4.000 mmol). Yield ~22%. The polycrystalline solid product differs in the hydration degree with respect to the single-crystalline sample, which contains 6 water molecules per formula unit. Average elemental analysis for $Na_2(P_4O_{12}N_2C_{10}H_{26})\cdot 8H_2O$ (MW = 680.31 g mol^{-1}). Calculated, %: C 17.65, H 6.22, N 4.12. Found, %: C 17.31, H 5.79, N 4.17.

K-HDTMP, $[K_2(HDTMP)(H_2O)_8]$. The quantities used were: solid HDTMP (0.984 g, 2.000 mmol) and KOH (0.224 g, 4.000 mmol). Yield ~20%. Elemental analysis for $K_2(P_4O_{12}N_2C_{10}H_{26})\cdot 8H_2O$ (MW = 712.53 g mol^{-1}). Calculated, %: C 16.85, H 5.94, N 3.93. Found, %: C 16.76, H 5.75, N 4.01.

Rb-HDTMP, $[Rb(HDTMP)(H_2O)_2\cdot 2H_2O]$. The quantities used were: solid HDTMP (0.098 g, 0.200 mmol in 10 mL DI water), RbOH (0.04 g, 0.400 mmol in 5 mL DI water), and EtOH precipitant (30 mL). Yield ~5%. Polycrystalline samples are biphasic with two different hydration degrees, with one of the phases corresponding to that of the single crystal sample. Average elemental analysis for $Rb(P_4O_{12}N_2C_{10}H_{27})\cdot 6H_2O$ (MW = 684.78 g mol^{-1}). Calculated, %: C 17.54, H 5.74, N 4.09. Found, %: C 17.08, H 5.01, N 4.10.

Cs-HDTMP, $[Cs(HDTMP)(H_2O)_2\cdot 2H_2O]$

Synthesis A. This method was followed to obtain good quality single crystals. Solid HDTMP acid (0.164 g, 0.300 mmol) was sonicated in 20 mL DI water. Then a solution of CsCl (0.112 g, 0.600 mmol of CsCl in 5 mL DI water) was added to it under stirring until a clear colorless solution was obtained. A small quantity of the resulting solution (2.5 mL) was transferred to a small (0.5 cm diameter) test tube and a volume of 35 mL EtOH was carefully layered on top of the aqueous phase with a Pasteur pipette, forming a double H_2O/

EtOH layer. The system was covered with Parafilm and left undisturbed for 2 weeks, after which large colorless needle-like crystals were formed. They were isolated by filtration, washed with EtOH and air-dried. Yield ~3%.

Synthesis B. This method was the same as the synthesis of all other **M-HDTMP** compounds. The quantities used were: solid HDTMP (0.164 g, 0.300 mmol in 20 mL DI water), CsCl (0.112 g, 0.6 mmol in 5 mL DI water), and EtOH precipitant (30 mL). Yield ~50%. Elemental analysis for $Cs(P_4O_{12}N_2C_{10}H_{27})\cdot 4H_2O$ (MW = 696.19 g mol^{-1}). Calculated, %: C 17.25, H 5.07, N 4.02. Found, %: C 17.13, H 4.89, N 4.10.

2.3 Instrumentation

Elemental analyses (C, H, N) were performed on a Perkin–Elmer 2400 analyzer. Thermogravimetric analysis (TGA) data were recorded on an SDT-Q600 analyzer from TA instruments. The temperature varied from RT to 900 °C at a heating rate of 10 °C min^{-1}. Measurements were carried out on the samples in open platinum crucibles under an air flow. Vibrational spectra were obtained with an ATR accessory coupled to a FTIR spectrometer (Perkin-Elmer FT 1760). All spectra were recorded in the range of 4000 to 500 cm^{-1} at a resolution of 4 cm^{-1} and 32 scans were accumulated.

Structural determinations. X-ray diffraction data were collected at room temperature from a single-crystal mounted atop a glass fiber with Paratone-N oil, with a Bruker SMART APEX II diffractometer using graphite-monochromated Mo-Kα (λ = 0.71073 Å) radiation. The structures were solved by employing SHELXTL direct methods and refined by full-matrix least squares on F^2, using the APEX2 software package.[51] All non-H atoms were refined with independent anisotropic displacement parameters. Hydrogen atoms were placed at calculated positions and refined using a riding model, except for the water and phosphonic acid O–H hydrogen atoms, which were located from the Fourier difference density maps and refined using a riding model with O–H distance restraints. The crystallographic details and CCDC reference codes of the crystal structures are summarized in Table 1.

Laboratory X-ray powder diffraction patterns and thermodiffraction data were collected on a PANalytical X'Pert Pro automated diffractometer in the Bragg–Brentano reflection configuration by using a Ge(111) primary monochromator (Cu $K_{\alpha 1}$) and an X'Celerator detector. Thermodiffractometric data for **M-HDTMP** were obtained for the samples using an Anton Paar TTK450 camera under static air. Data were collected at different temperature intervals, from room temperature up to 250 °C, for **Li-HDTMP-4W**, and at 150 °C for the other **M-HDTMP** derivatives. A heating rate of 5 °C min^{-1} and a delay time of 5 minutes to ensure thermal stabilization were used. The data acquisition range was 4–70° (2θ), with a step size of 0.017° and an equivalent counting time of 230 s per step. Crystallite sizes were calculated using the Williamson–Hall plot using HighScore Plus v4.6a software [PANalytical B.V.] and LaB_6 as the standard for the determination of the instrumental resolution function.

Table 1 Selected crystallographic data for the **M-HDTMP** (M = Li, Na, K, Rb and Cs) compounds

Phase	Li-HDTMP-4W	Li-HDTMP-0W	Na-HDTMP	K-HDTMP	Rb-HDTMP	Cs-HDTMP
Space group	$P\bar{1}$	$P\bar{1}$	$P\bar{1}$	$P2_1/c$	$C2/c$	$P\bar{1}$
Chemical formula	$Li_2P_4O_{16}N_2C_{10}H_{34}$	$Li_2P_4O_{12}N_2C_{10}H_{26}$	$Na_2P_4O_{23}N_2C_{10}H_{48}$	$K_2P_4O_{20}N_2C_{10}H_{42}$	$RbP_4O_{16}N_2C_{10}H_{35}$	$CsP_4O_{16}N_2C_{10}H_{35}$
Formula mass (g mol)	576.16	504.10	734.36	712.53	648.75	696.19
λ (Å)	0.71073	0.18972	0.71073	0.71073	0.71073	0.71073
a (Å)	5.9728(6)	5.9014(4)	7.66820(10)	7.71780(10)	6.0257(5)	6.0072(2)
b (Å)	9.4557(9)	9.2693(7)	11.53350(10)	33.0373(4)	14.1011(7)	7.6864(2)
c (Å)	11.0182(11)	9.5123(7)	18.0768(2)	11.75770(10)	28.762(2)	14.8250(4)
α (°)	74.418(7)	85.902(4)	97.3780(10)	90.00	90.00	86.677(2)
β (°)	76.170(7)	77.676(5)	94.7920(10)	103.7090(10)	94.816(3)	78.906(2)
γ (°)	84.313(7)	85.588(6)	101.7050(10)	90.00	90.00	67.611(2)
V (Å^3)	581.622(10)	506.04(8)	1542.61(3)	2912.52(6)	2435.25(6)	621.01(3)
Crystal size (mm)	0.22 × 0.05 × 0.04	—	0.45 × 0.22 × 0.03	0.50 × 0.20 × 0.05	0.50 × 0.21 × 0.09	0.10 × 0.07 × 0.03
Z	1	1	2	4	4	1
ρ_{calc} (g cm^{-3})	1.645	1.568	1.526	1.782	1.721	1.862
2θ range (°)	2.58–24.54	0.187–13.501	1.82–31.03	1.89–30.02	1.41–33.45	2.87–27.91
Data/restraints/parameters	1719/7/175	1428/94/33	7729/28/457	7448/22/409	3984/10/189	2722/8/176
No. of reflections	10 054	2254	9784	8877	4773	3748
Independent reflections [$I > 2\sigma(I)$]	1693	—	7729	7448	3984	2722
R_{wp}	—	0.0115	—	—	—	—
R_p	—	0.0220	—	—	—	—
R_F	—	0.0427	—	—	—	—
GoF	0.991	—	1.052	1.036	1.039	1.024
R factor [$I > 2\sigma(I)$]	[a] R_1 = 0.0578, [a] wR_2 = 0.1399	—	[a] R_1 = 0.0368, [a] wR_2 = 0.0905	[a] R_1 = 0.0287, [a] wR_2 = 0.0666	[a] R_1 = 0.0328, [a] wR_2 = 0.0791	[a] R_1 = 0.0344, [a] wR_2 = 0.0676
R factor (all data)	[a] R_1 = 0.0904, [a] wR_2 = 0.1595	—	[a] R_1 = 0.0527, [a] wR_2 = 0.0981	[a] R_1 = 0.0393, [a] wR_2 = 0.0713	[a] R_1 = 0.0436, [a] wR_2 = 0.0838	[a] R_1 = 0.0580, [a] wR_2 = 0.0759
CCDC code	1584820	1584815	1584819	1584817	1584816	1584818

[a] $R_1(F) = \sum||F_o| - |F_c||/\sum|F_o|$; $wR_2(F^2) = [\sum w(F_o^2 - F_c^2)^2/\sum F^4]^{1/2}$.

Synchrotron X-ray powder diffraction data for **Li-HDTMP-0W** were collected with a beam energy of 65.341 keV [λ = 0.18972(1) Å] at the ID15A beamline at the ESRF, Grenoble (France). The beam was monochromated with a double bent Laue monochromator giving a band pass of *ca.* 4×10^{-3} $\Delta E/E$. Diffraction patterns were collected in transmission geometry using a Pilatus3 X CdTe 2 M hybrid photon counting detector with a pixel size of 172 × 172 μm^2. The detector distance, calibrated with a pattern of CeO_2, was determined to be 1000 mm. The intensity profile was corrected for the background contribution, polarization of the X-rays and detector geometry, response, and transparency. Five images were collected with an acquisition time of 8 s per image, over the angular range of 0.95–13.50° (2θ). The glass capillary, 0.7 mm in diameter, was rotated during data collection to improve diffracting particle statistics. The powder pattern was autoindexed using the program DICVOL[52] in a triclinic cell with parameters quite similar to those of the as-synthesized sample. The crystal structure of **Li-HDTMP-0W** was solved by Rietveld refinement[53] using as a starting model the crystal structure of **Li-HDTMP-4W**, available from single crystal determination. The refinement was carried out by using the GSAS package[54] with soft constraints to maintain the chemically reasonable geometries for the phosphonate, amine groups and alkyl chains: /PO_3C tetrahedron/ P–O (1.53(1) Å), P–C (1.80(1) Å), O···O (2.55(2) Å), and O···C (2.73(2) Å); /$N(CH_2)_3$ amine group/ N–C (1.50(1) Å) and C···C (2.45(2) Å); and /alkyl chain/ C–C (1.50(1) Å) and $C_{chain}\cdots C_{chain}$ (2.50(2) Å). The final weight factor for the soft constraints was 15 and two isotropic atomic displacement parameters were refined, one for P atoms and the second for N, C and O atoms. For the Li atom an isotropic displacement parameter was fixed (0.04 $Å^2$). The final Rietveld plot is given in Fig. S1 (ESI†) and the most relevant crystallographic data are presented in Table 1.

Proton conductivity studies. Impedance data were collected on ~1 mm thick cylindrical pellets (~5 mm in diameter), which were obtained by pressing ~40 mg of sample at 250 MPa for 2 min between porous C electrodes (Sigracet, GDL 10 BB, no Pt). The sample cell was placed inside a temperature and humidity controlled chamber ESPEC SH-222 connected to an AUTOLAB PGSTAT302N analyzer over the frequency range from 20 Hz to 10^5 Hz with an applied voltage of 0.35 V. To equilibrate the water content, the pellets were first preheated (0.2 °C min^{-1}) from 25 to 80 °C at a relative humidity (RH) of 95%. Impedance spectra were recorded upon cooling using a stabilization time of 5 h at 20 °C intervals and variable relative humidity values (60% and 95% RH). Water condensation on the sample was avoided by reducing first the relative humidity before decreasing the temperature. All measurements were electronically controlled using the winDETA package of programs.[55]

Solid-state NMR. ^{1}H MAS (magic angle spinning) NMR spectra were obtained using a Bruker Ascend-600 spectrometer equipped with a 2.5 mm MAS probe with an operating frequency for protons of 600.09 MHz. ^{1}H spectra were recorded at a spinning rate of 30 kHz, with a pulse width of 2 μs, a dwell time of 6.50 μs and a delay of 3 s. ^{1}H chemical shifts were indirectly referenced by using adamantane as an external reference. The deconvolution of the ^{1}H MAS-NMR spectra was carried out using the DMFIT program to obtain the different components and their contributions.[56]

3. Results and discussion

In general, polycrystalline samples display higher water content than their corresponding single crystals. This excess of water is related to the presence of other more hydrated polycrystalline phases (*e.g.* **Na-** and **Rb-HDTMP**) coexistent with their corresponding single crystal phases, as can be inferred from a comparison between the XRD patterns simulated from the single crystals and the XRD patterns of the polycrystalline samples (Fig. S2-upper†). However, the water content in **Li-**, **K-** and **Cs-HDTMP** derivatives is in good agreement with that of their corresponding single crystals (Fig. S2†).

All new compounds were characterized by ATR-IR spectroscopy (Fig. S2-lower†), which allowed differentiation of the different structural modes of the phosphonate groups. Vibrations of the P–OH moiety appear in the 890–940 cm^{-1} region. Peaks around 1040 cm^{-1} and 1250 cm^{-1} are assigned to the asymmetric P═O stretching. The $-PO_3$ stretching appears as a strong band in the 1085–1165 cm^{-1} region, whereas the–PO_3 bending shows up in the 400–600 cm^{-1} region. The O–H stretching vibration is noted as a multitude of broad bands in the 3200–3600 cm^{-1} region, while bending vibrations are at ~1640 cm^{-1}, all originating from bound or lattice water.

3.1 Crystal structures of "free" HDTMP and Li-HDTMP compounds

HDTMP. The crystal structure of the free HDTMP acid has been reported by our group elsewhere.[57] It crystallizes as an anhydrous form and is located on an inversion center within the triclinic ($P\bar{1}$) crystal lattice. Two phosphonate groups (one on each side) of the zwitterionic molecule are singly deprotonated ($-PO_3H^-$), whereas the other two are fully protonated ($-PO_3H_2$). The tertiary N atoms are also protonated. This is a common phenomenon in the crystal structures of amino-bis(methylenephosphonates).[58] An extended 3D-network is formed by H-bonding between the phosphonate groups and NH^+ moieties (Fig. S3, Table S1 in the ESI†).

Li-HDTMP compounds. The crystal structure of **Li-HDTMP-4W**, solved by single-crystal X-ray diffraction, contains an inversion center within the triclinic ($P\bar{1}$) crystal lattice (Fig. 1). All phosphonate moieties of the HDTMP ligand are singly deprotonated ($-PO_3H^-$). Both N atoms are protonated; hence, the entire HDTMP molecule is dianionic. Lithium is tetrahedrally coordinated by four oxygen atoms, originating from two water molecules and two phosphonate oxygen atoms from two different HDTMP molecules, thus creating rings built up of two ligand molecules and two metal ions. The rings are stabilized by H-bonds between phosphonate groups and extend into 1D-ribbons (Fig. 2a).

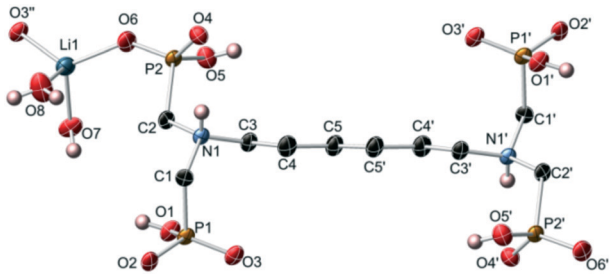

Fig. 1 Thermal ellipsoid plot (50% probability) of **Li-HDTMP**, showing the tetrahedral coordination sphere around the Li^+ ion (C–H hydrogen atoms are not shown for clarity). Symmetry operators: (′) $x + 1/2, -y, -z + 1$; (″) $x, y + 1, z$.

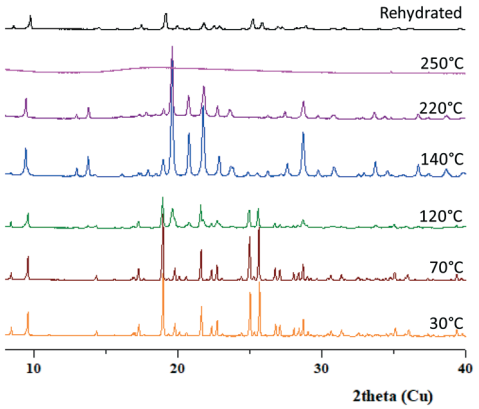

Fig. 3 Thermodiffraction patterns for the **Li-HDTMP-4W** compound.

These ribbons are connected further by H-bonds to the NH^+ moieties and H_2O molecules (Fig. 2b, and Table S1†).

The thermodiffractometric study (Fig. 3) revealed that the solid **Li-HDTMP-4W** maintains its stability up to ~120 °C. By further heating, a second phase clearly develops from 140 °C and remains as the unique crystalline phase up to 220 °C.

As demonstrated below, this new phase is anhydrous (**Li-HDTMP-0W**). The water is lost in a stepwise fashion between 100 °C and 220 °C (calculated, 15.2%; found, 15.1%). An additional weight loss, observed in the range of 220–300 °C, is attributed to partial condensation of P–OH groups as compared with the thermal behaviour of the free phosphonic acid (Fig. 4). This process induces amorphization before decomposition, which takes place at ~300 °C. Importantly, **Li-HDTMP-0W** is reversibly hydrated to the initial phase by long exposure to ambient conditions or short exposure (5 h) at 80 °C and 95% RH.

The crystal structure of **Li-HDTMP-0W**, Fig. 5, can be viewed as a result of the condensation of the ribbon-like chains into a 2D framework, in which the tetrahedral coordination of the lithium atoms is preserved by increasing the connectivity of the phosphonate groups with respect to the metal ions. In this new structure, 16-membered rings are created through formation of edge-sharing LiO_6 dimers extended along the *a*-axis.

3.2 Crystal structure of M-HDTMP (M = Na^+, K^+, Rb^+ and Cs^+)

Na-HDTMP crystallizes in the triclinic ($P\bar{1}$) crystal system, with the ligand moiety being located on a general position and all phosphonate groups being singly deprotonated ($-PO_3H^-$) (Fig. 6). Both N atoms are protonated; hence, the entire HDTMP molecule is dianionic. There are three crystallographically independent Na^+ ions in the lattice. Two of these (Na1 and Na3) are located on inversion centers. Na1 and Na2 are 6-coordinated, the former by two phosphonate O-atoms (from two different ligand molecules) and four water O-atoms, and the latter by one phosphonate O-atom and four water O-atoms. Na1 and Na2 are bridged by H_2O molecules and coordinate to HDTMP moieties to form a 1D-ribbon (Fig. 6) of edge- and face-sharing octahedra. Na3 serves as a counter ion in the form of octahedral $[Na(H_2O)_6]^+$. The 1D-ribbons are

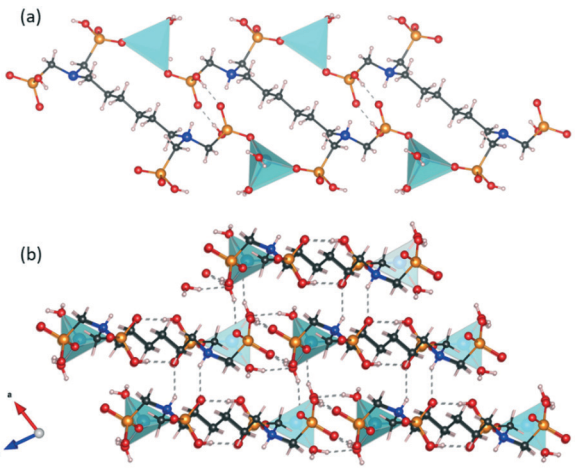

Fig. 2 View of the **Li-HDTMP-4W** structure showing (a) the 1D-ribbon motifs and (b) packing of the 1D-ribbon with H-bond interactions (2.7 < D–H···A < 2.99 Å) marked. K. Momma and F. Izumi, VESTA 3 for three-dimensional visualization of crystal, volumetric and morphology data, *J. Appl. Crystallogr.*, 2011, **44**, 1272–1276.

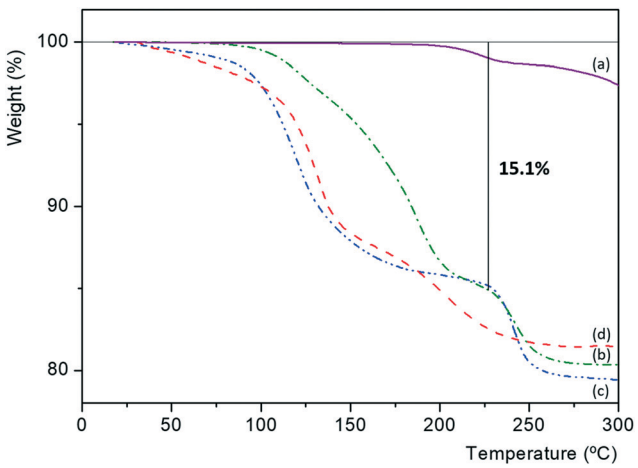

Fig. 4 Thermal analysis for compounds, (a) HDTMP, (b) **LiHDTMP-4W**, (c) **Li-HDTMP** after impedance measurements, and (d) rehydrated **Li-HDTMP-0W**.

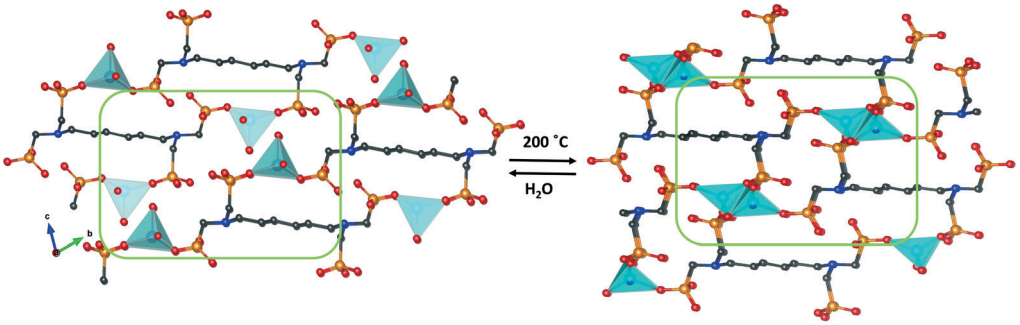

Fig. 5 Reversible structural transformation of **Li-HDTMP** compounds upon carrying out dehydration–rehydration cycles.

connected to each other and the $[Na(H_2O)_6]^+$ counterions by H-bonding *via* multiple lattice H_2O molecules (Fig. 6).

K-HDTMP exhibits a monoclinic lattice ($P2_1/c$) where the ligand is also dianionic as in the case of **Na-HDTMP** (Fig. 7a). There are two crystallographically independent K^+ ions in the lattice: K1 is heptacoordinated by three phosphonate O-atoms (from two different ligand molecules) and four water O-atoms, and K2 is hexacoordinated by one phosphonate O-atom and five water O-atoms. K1 and K2 form face-sharing dimers through three oxygen atoms from two water molecules (O13 and O14) and one phosphonate group (O2). These dimers are connected to each other by one bridged H_2O molecule (O17) giving rise to chains interconnected by the HDTMP ligand (Fig. 7b). The zig-zag layers generated are packed through H-bonds, assisted by lattice water molecules located between them.

In the monoclinic lattice ($C2/c$) of **Rb-HDTMP**, the Rb^+ ions are located on a C_2 axis and are octacoordinated by six phosphonate O-atoms (from four different ligand molecules) and two water O-atoms. Similar to K^+, the Rb^+ ions in **Rb-HDTMP** form sheets, which are connected to each other by dianionic HDTMP ligand molecules. In contrast to the K-salt, however, the sheet is formed by isolated phosphonate-bridged Rb^+ polyhedra (Fig. 8). In this framework, the HDTMP ligand also connects sheets into a pillared layered structure with the lattice water situated inside the interlayer space giving rise to an H-bond network (Fig. 8).

Within the triclinic ($P\bar{1}$) lattice of **Cs-HDTMP**, the Cs^+ ions are located on an inversion center and are octacoordinated by six phosphonate O-atoms (from four different ligand molecules) and two water O-atoms. Sheets are formed by edge-sharing Cs^+ polyhedra bridged by phosphonate groups (Fig. 9). The sheets are similarly connected by doubly

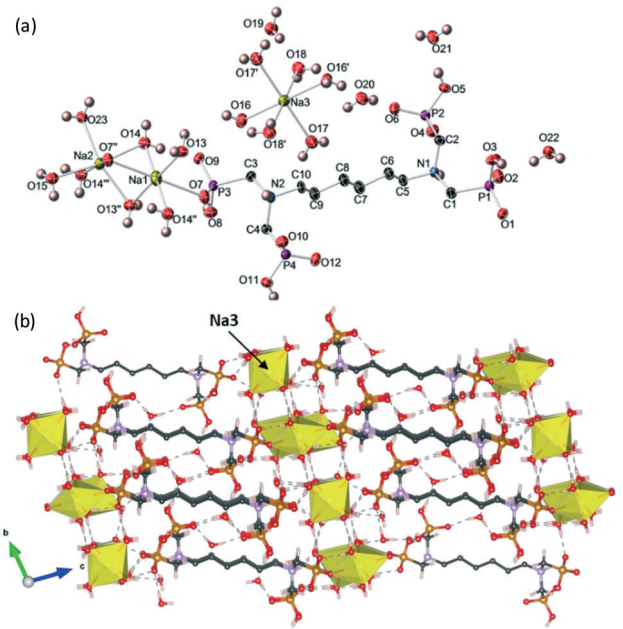

Fig. 6 (a) Thermal ellipsoid plot (80% probability) of **Na-HDTMP** showing the coordination sphere around the Na^+ ions. Symmetry operators: (′) $-x + 2, -y + 1, -z + 2$; (″) $-x, -y, -z + 2$; (‴) $-x - 1, -y, -z + 2$. (b) 3D-packing of the 1D-ribbons in **Na-HDTMP** (C–H hydrogen atoms are not shown for clarity).

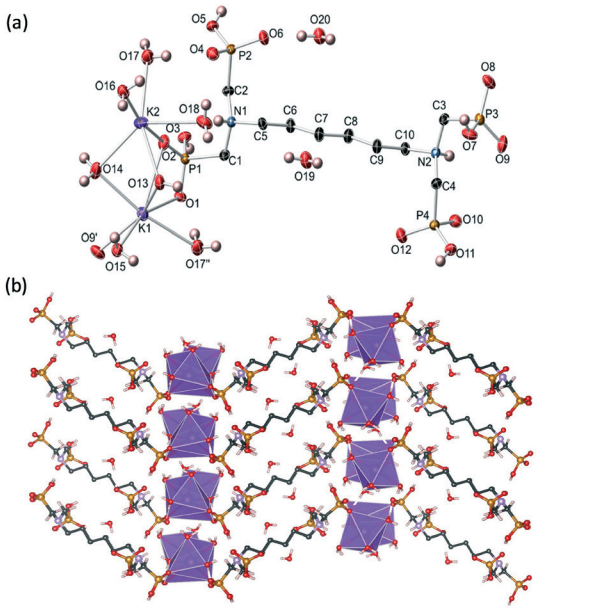

Fig. 7 (a) Thermal ellipsoid plot (80% probability) of **K-HDTMP**, showing the coordination sphere around the K^+ ions and connectivity of the chains. Symmetry operators: (′) $-x + 1, y - 1/2, -z + 3/2$; (″) $x + 1, y, z$. (b) View of the layered structure of **K-HDTMP** (C–H hydrogen atoms are not shown for clarity).

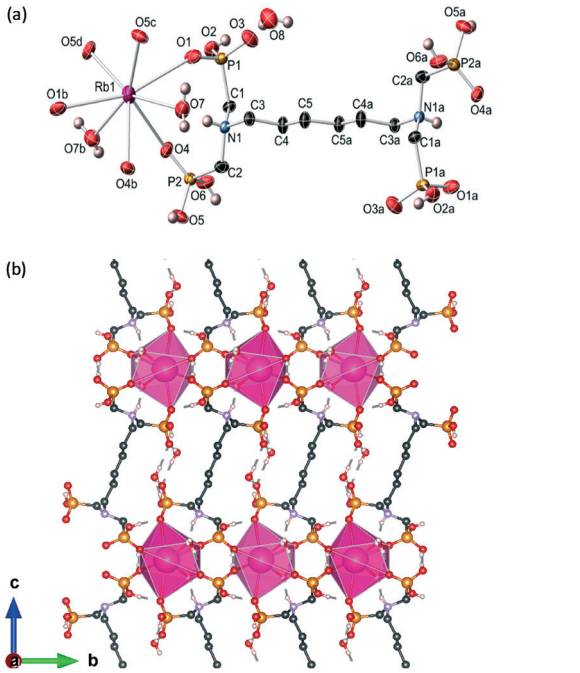

Fig. 8 (a) Thermal ellipsoid plot (50% probability) of **Rb-HDTMP**, showing the coordination sphere around the Rb ion (only one of the two disordered O7 atoms is shown for clarity). Symmetry operators: (a) $-x + 2, y - 1, -z + 1$; (b) $-x + 1, y, -z + 1/2$; (c) $-x + 1/2, y - 1/2, z$; (d) $-x + 1/2, y - 1/2, -z + 1/2$. (b) View of the pillared layered structure of **Rb-HDTMP** (C–H hydrogen atoms are not shown for clarity).

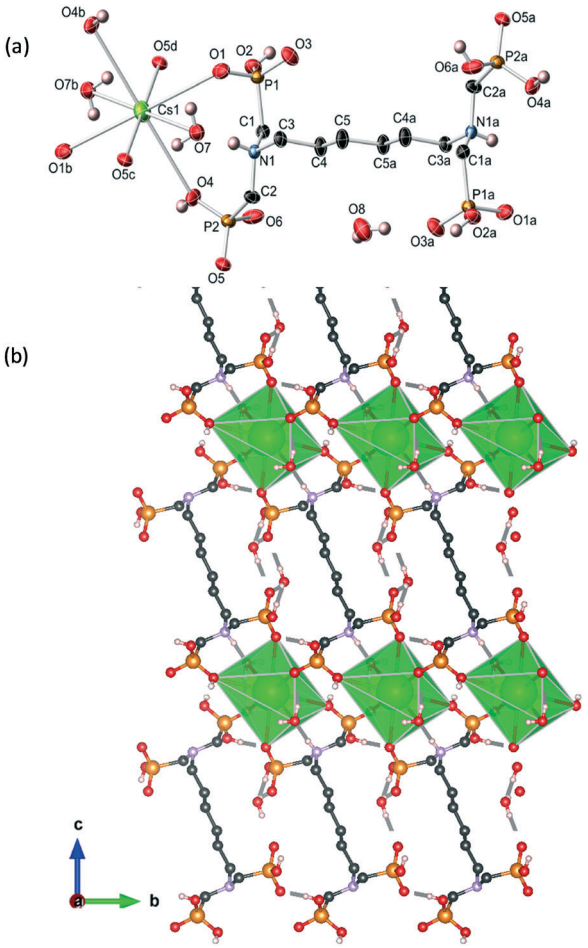

Fig. 9 (a) Thermal ellipsoid plot (50% probability) of **Cs-HDTMP**, showing the coordination sphere around the Cs ion. Symmetry operators: (a) $-x, y - 1, -z + 2$; (b) $-x + 1, -y + 2, -z + 1$; (c) $-x + 1, -y + 1, -z + 1$; (d) $x, y + 1, z$. (b) View of the pillared layered structure of **Cs-HDTMP** (C–H hydrogen atoms are not shown for clarity).

deprotonated HDTMP ligand molecules into a pillared-layered structure (Fig. 9) containing H-bonded lattice water.

The thermal behaviour of compounds **M-HDTMP** (M = Na, K, Rb, and Cs) follows a similar dehydration pattern before decomposition at *ca.* 240 °C (Fig. S4†). The Na^+ salt showed the highest divergence in hydration with respect to the single crystal (observed, 22.42%; calculated 16.76%). The weight loss observed for **K-HDTMP**, 20.40%, agrees well with the calculated value for full dehydration of the compound (calculated 20.22%). **Rb-HDTMP** shows several consecutive weight losses between RT and 240 °C. The observed weight loss, 12.92%, is slightly higher than the calculated value, taking into account the composition of the single crystal analysed (11.11%). As corroborated by thermodiffraction (Fig. S5†), the polycrystalline sample lost labile water below 80 °C. At this temperature, the X-ray powder diffraction pattern agrees well with the one simulated from the single crystal data. Further heating leads to the amorphization of the solid. **Cs-HDTMP** starts losing water at ~100 °C, with a total weight loss corresponding to 4 water molecules (observed 9.57%, calculated 10.34%).

Despite the observed trend of increasing ligand denticity towards larger M^+ cations, a direct relationship between the M^+ radius and the average M–O bond distance is maintained (Fig. S6†). The complexity of the **M-HDTMP** structures deserves further discussion. The effect of the alkali metal ionic radii is reflected not only on the M–O bond distances (either with water or phosphonate oxygen atoms), but also on the coordination number of the metal center. The tetrahedral Li^+ cations in the structure of **Li-HDTMP** are 4-coordinated (by two different HDTMP ligands and two water molecules). The structure adopted is 1D "ribbon" or "slab". The Na^+ ions in the structure of **Na-HPAA** are 6-coordinated (by one phosphonate oxygen and five water molecules). The structure adopted is 1D with $Na(H_2O)_6^+$ counter ions for charge balance. The K^+ cations in the 3D structure of **K-HDTMP** are 6-coordinated (by one phosphonate oxygen and five water molecules) and 8-coordinated (by three phosphonate oxygen atoms and five water molecules). The Rb^+ cations in the 3D structure of **Rb-HDTMP** are 8-coordinated (by six phosphonate oxygen atoms and two water molecules). Finally, the largest cation Cs^+ is 10-coordinated in the 3D structure of **Cs-HDTMP** (four HDTMP ligands, eight phosphonate oxygen atoms and two water molecules). These observations are in line with previous reports on alkali metal-HPAA[59] and alkaline-earth metal HPAA[47,60–64] (HPAA = hydroxyphosphonoacetic acid) systems and/or alkaline-earth metal AMP[65–67] (AMP = amino-*tris*(methylenephosphonic acid)) systems.

3.3 Proton conduction

The structural features exhibited by these compounds, with extended H-bonding networks, make them potential candidates as proton conductors. Preliminary stability tests performed at high RH values showed that all compounds except the lithium derivative are highly hygroscopic materials. Therefore only the proton conductivity properties of **HDTMP** and **Li-HDTMP** solids were studied. The impedance spectra at different temperatures and RH for **HDTMP** and **Li-HDTMP** compounds are shown in Fig. S7.† The total pellet resistance, R_T, was obtained from the intercept of the spike and/or the arc (low-frequency end) on the Z' axis. The Arrhenius plots, Fig. 10, show the overall pellet conductivities for **HDTMP** and **Li-HDTMP** compounds between 25 and 80 °C. As can be seen, the proton conductivity of the "free" **HDTMP** phosphonic acid dramatically increases by nearly three orders of magnitude with the RH from 9.2×10^{-7} S cm^{-1} (60%, 80 °C) to 2.2×10^{-4} S cm^{-1} (95%, 80 °C). It has been reported that the proton conductivity of phosphonic acids is higher for crystalline than amorphous phases. This behavior is correlated with the self-assembly of phosphonic groups generating regions with high concentration of H-bonds and hence, providing high proton conductivity values in ordered compounds.[68] Fig. S3† displays the packing of the ligand molecules where hydrogen-bond interactions are apparent along the *a*-axis. In this case, not only the phosphonic groups are involved but also the protonated amine groups contribute to the extended network. As already demonstrated,[68] the structural arrangement in crystalline phosphonic acids may facilitate the adsorption of small amounts of water (<1% from TG for **HDTMP**) upon increasing the relative humidity, giving rise to extended H-bond networks that significantly enhance proton conductivity. The low activation energy (0.29 eV) determined from the Arrhenius plot (Fig. 10) indicates that a Grotthuss proton transfer mechanism operates at high humidity.[69] The post-impedance powder diffraction pattern of **HDTMP** did not show any structural change (Fig. S8†).

The as-synthesized **Li-HDTMP-4W** shows higher proton conductivity values (7.6×10^{-4} S cm^{-1} at 80 °C and 95% RH) than the free **HDTMP** which is attributed to the presence of coordinated water in the structure of the former, thus contributing to establishing additional H-bond interactions with the acidic groups of the ligand, and hence, more extended proton transport pathways (see Table S1†) are formed in the lithium derivative structure. The activation energy value found for this compound (Fig. 10) is 0.41 eV at 95% RH and increases slightly up to 0.54 eV at 60% RH, which suggests a gradual change in the proton transfer from the Grotthuss to the vehicle mechanism. **Li-HDTMP-0W** rehydrates to **Li-HDTMP-4W** upon preheating the sample at 80 °C and 95% RH for 5 h, therefore the conductivity measurements correspond to the fully hydrated compound (Fig. S9†). Interestingly, this sample displays a proton conductivity value almost one order of magnitude higher than that of the as-synthesized **Li-HDTMP-4W** (5×10^{-3} S cm^{-1} *versus* 7.6×10^{-4} S cm^{-1} at 80 °C and 95% RH). In order to obtain a better understanding of this behavior, Rietveld-determined particle size, solid state ^{1}H-MAS-NMR and TG analyses were performed. After impedance measurements, a half particle size reduction was determined for both samples, from ~1400 Å to ~700 Å for the as-synthesized sample and from ~1200 Å to ~600 Å for the rehydrated **Li-HDTMP-0W**, resulting in pellets with similar compactions (~85%).

^{1}H-MAS-NMR spectra for all **Li-HDTMP** compounds were collected. Fig. 11 shows the spectra for **Li-HDTMP-4W** as synthesized (a), **Li-HDTMP-0W** (b) and rehydrated **Li-HDTMP-0W** (c). They consist of broad bands that can be deconvoluted into several components. Together with the signals corresponding to the –CH_2– groups (Table S2†), the bands appearing in the spectra at 8.6 ppm and 11.0 ppm are assigned to P–OH and N–H^+ groups, respectively,[70] whereas that at ~5.0 ppm correlates with bound water.[71] For all **Li-HDTMP** compounds, the post-impedance spectra were quite similar, confirming that they correspond to the same fully hydrated structure.

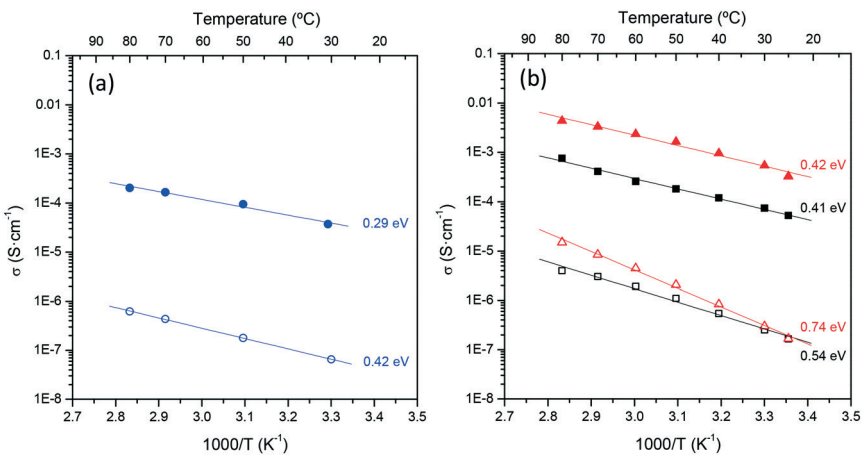

Fig. 10 Arrhenius plots for: (a) **HDTMP** acid and (b) as-synthesized **Li-HDTMP-4W** (squares) and rehydrated **Li-HDTMP-0W** (triangles) at 60% RH (empty) and 95% RH (filled).

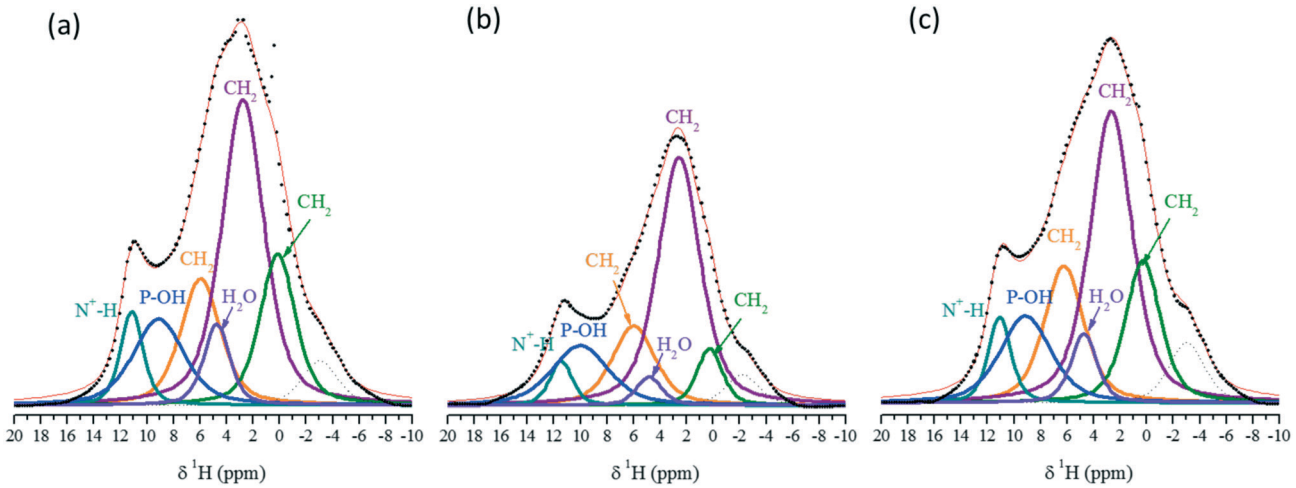

Fig. 11 Solid state ^{1}H-MAS-NMR spectra showing the fitting to several components for (a) **Li-HDTMP-4W**, (b) **Li-HDTMP-0W** and (c) rehydrated **Li-HDTMP-0W**. The bands located near −3 ppm are due to the signal probe.

However, the TG curves (Fig. 4) reveal subtle variations in the water loss, which suggest that a change in water interactions occurred in the framework. The rehydration process implies the breaking of the P–O(H)–Li bonds and its transformation P–OH + Li–OH_2 (Fig. 5). It can be speculated that a memory effect is preserved in the rehydrated **Li-HDTMP-0W** sample making the reformation of the P–O(H)–Li bonds easier and hence, leading to changes in the acidity of acid groups and water mobility that would justify the changes in the conductivity.

Conclusions

Reactions of the flexible tetraphosphonate ligand **HDTMP** with the alkali metal ion series generate a cation size-induced structural diversity from monodimensional solids (Li^+ and Na^+) through layered (K^+) to pillared-layered (Rb^+ and Cs^+) structures with water exhibiting pleiotropic roles: (a) as a metal-bound terminal ligand, (b) as a bridging ligand, and (c) as a H-bonding donor and acceptor. These multiple roles give rise to different proton transport pathways. While the Na^+- to Cs^+-salts are highly hygroscopic materials, the lithium derivative shows high thermal stability and reversible dehydration/rehydration between 25 °C and 200 °C. Through this process, the proton conductivity is enhanced by almost one order of magnitude, reaching a value of 5×10^{-3} S cm^{-1} (80 °C and 95% RH). This effect is attributed to subtle changes in the interaction of water molecules and acidity within the crystalline structure.

Conflicts of interest

There are no conflicts to declare.

Acknowledgements

The work at UoC was supported by grants from the Research Committee of the University of Crete, ELKE, (Grant #KA 3806). The work at UMA was funded by MAT2016-77648-R research grant (Spain) and Junta de Andalucía (Spain) P12-FQM-1656. A.I.M. thanks the Ministry of Economy and Competitiveness for a Ramon y Cajal contract (RyC2015-17870). The work at WMU was supported by the US National Science Foundation under Grant No. CHE-1404730.

Notes and references

1 *Metal Phosphonate Chemistry: From Synthesis to Applications*, ed. A. Clearfield and K. D. Demadis, Royal Society of Chemistry, Cambridge, U.K., 2012.
2 *Tailored Organic-Inorganic Materials*, ed. E. Brunet, J. L. Colón and A. Clearfield, John Wiley & Sons, Inc., New York, U.S.A., 2015.
3 M. T. Wharmby, J. P. S. Mowat, S. P. Thompson and P. A. Wright, *J. Am. Chem. Soc.*, 2011, **133**, 1266–1269.
4 S. R. Miller, G. M. Pearce, P. A. Wright, F. Bonino, S. Chavan, S. Bordiga, I. Margiolaki, N. Guillou, G. Ferey, S. Bourrelly and P. L. Llewellyn, *J. Am. Chem. Soc.*, 2008, **130**, 15967–15981.
5 K. Maeda, *Microporous Mesoporous Mater.*, 2004, **73**, 47–55.
6 R. F. Mendes, D. Ananias, L. D. Carlos, J. Rocha and F. A. Almeida Paz, *Cryst. Growth Des.*, 2017, **17**, 5191–5199.
7 G.-T. Wang, Z.-Y. Tang, H.-T. Zhou and P. Zou, *Polyhedron*, 2016, **117**, 259–264.
8 A. Donnadio, M. Nocchetti, F. Costantino, M. Taddei, M. Casciola, F. da Silva Lisboa and R. Vivani, *Inorg. Chem.*, 2014, **53**, 13220–13226.
9 S. Begum, Z. Wang, A. Donnadio, F. Costantino, M. Casciola, R. Valiullin, C. Chmelik, M. Bertmer, J. Kärger, J. Haase and H. Krautscheid, *Chem. – Eur. J.*, 2014, **20**, 8862–8866.
10 S.-S. Bao, G. K. H. Shimizu and L.-M. Zheng, *Coord. Chem. Rev.*, 2017, DOI: 10.1016/j.ccr.2017.11.029, in press.
11 S.-S. Bao, N.-Z. Li, J. M. Taylor, Y. Shen, H. Kitagawa and L.-M. Zheng, *Chem. Mater.*, 2015, **27**, 8116–8125.

12 J. M. Taylor, R. K. Mah, I. L. Moudrakovski, C. I. Ratcliffe, R. Vaidhyanathan and G. K. H. Shimizu, *J. Am. Chem. Soc.*, 2010, **132**, 14055–14057.
13 Z. H. Fard, N. E. Wong, C. D. Malliakas, P. Ramaswamy, J. M. Taylor, K. Otsubo and G. K. H. Shimizu, *Chem. Mater.*, 2018, **30**, 314–318.
14 J. Zhang, L. Chen, D. Gui, H. Zhang, D. Zhang, W. Liu, G. Huang, J. Diwu, Z. Chai and S. Wang, *Dalton Trans.*, 2018, **47**, 5161–5165.
15 K. D. Demadis, C. Mantzaridis and P. Lykoudis, *Ind. Eng. Chem. Res.*, 2006, **45**, 7795–7800.
16 M. Papadaki and K. D. Demadis, *Comments Inorg. Chem.*, 2009, **30**, 89–118.
17 R. M. P. Colodrero, G. K. Angeli, M. Bazaga-Garcia, P. Olivera-Pastor, D. Villemin, E. R. Losilla, E. Q. Martos, G. B. Hix, M. A. G. Aranda, K. D. Demadis and A. Cabeza, *Inorg. Chem.*, 2013, **52**, 8770–8783.
18 S. A. Umoren and M. M. Solomon, *J. Environ. Chem. Eng.*, 2017, **5**, 246–273.
19 D.-M. Zang, D.-K. Cao and L.-M. Zheng, *Inorg. Chem. Commun.*, 2011, **14**, 1920–1923.
20 A. Mesbah, S. Jacques, E. Rocca, M. François and J. Steinmetz, *Eur. J. Inorg. Chem.*, 2011, 1315–1321.
21 A. Popa, C.-M. Davidescu, N. Petru, I. Gheorghe, A. Katsaros and K. D. Demadis, *Ind. Eng. Chem. Res.*, 2008, **47**, 2010–2017.
22 A.-L. Alanne, M. Tuikka, K. Tnsuaadu, M. Ylisirniö, L. Hämäläinen, P. Turhanen, J. Vepsäläinen and S. Peräniemi, *RSC Adv.*, 2013, **3**, 14132–14138.
23 E. Barouda, K. D. Demadis, S. Freeman, F. Jones and M. I. Ogden, *Cryst. Growth Des.*, 2007, **7**, 321–327.
24 Z. Amjad and A. Kweik, *Phosphorus Res. Bull.*, 2015, **30**, 19–25.
25 Z. Amjad, R. T. Landgraf and J. L. Penn, *Int. J. Corros. Scale Inhib.*, 2014, **3**, 35–47.
26 Q. Luo, *Ind. Eng. Chem. Res.*, 2000, **39**, 3249–3254.
27 K. D. Demadis, E. Mavredaki and M. Somara, *Ind. Eng. Chem. Res.*, 2011, **50**, 13866–13876.
28 K. E. Papathanasiou, P. Turhanen, S. I. Brückner, E. Brunner and K. D. Demadis, *Sci. Rep.*, 2017, **7**, 4743.
29 R. W. Sparidans, I. M. Twiss and S. Talbot, *Pharm. World Sci.*, 1998, **20**, 206–213.
30 F. Cheng and E. Oldfield, *J. Med. Chem.*, 2004, **47**, 5149–5158.
31 G. De Rosa, G. Misso, G. Salzano and M. Caraglia, *J. Drug Delivery*, 2013, 637976.
32 K. Moedritzer and R. R. Irani, *J. Org. Chem.*, 1966, **31**, 1603–1607.
33 P. B. Iveson, M. P. L. Lowe and J. C. Lockhart, *Polyhedron*, 1993, **12**, 2313–2323.
34 E. D. Naydenova, P. T. Todorov and K. D. Troev, *Amino Acids*, 2010, **38**, 23–30.
35 D. Villemin and M. A. Didi, *Orient. J. Chem.*, 2015, **31**, 1–12.
36 N. Stock and T. Bein, *Angew. Chem., Int. Ed.*, 2004, **43**, 749–752.
37 N. Stock, A. Stoll and T. Bein, *Microporous Mesoporous Mater.*, 2004, **69**, 65–69.
38 N. Stock, N. Guillou, J. Senker, G. Férey and T. Bein, *Z. Anorg. Allg. Chem.*, 2005, **631**, 575–581.
39 N. Stock, M. Rauscher and T. Bein, *J. Solid State Chem.*, 2004, **117**, 642–647.
40 F. Costantino, T. Bataille, N. Audebrand, E. Le Fur and C. Sangregorio, *Cryst. Growth Des.*, 2007, **7**, 1881–1888.
41 R. Vivani, F. Costantino, U. Costantino and M. Nocchetti, *Inorg. Chem.*, 2006, **45**, 2388–2390.
42 R. M. P. Colodrero, A. Cabeza, P. Olivera-Pastor, A. Infantes-Molina, E. Barouda, K. D. Demadis and M. A. G. Aranda, *Chem. – Eur. J.*, 2009, **15**, 6612–6618.
43 K. D. Demadis, E. Barouda, R. G. Raptis and H. Zhao, *Inorg. Chem.*, 2009, **48**, 819–821.
44 G.-L. Zheng, J.-F. Ma and J. Yang, *J. Chem. Res.*, 2004, 387–388.
45 R. M. P. Colodrero, P. Olivera-Pastor, E. R. Losilla, M. A. G. Aranda, L. León-Reina, M. Papadaki, A. C. McKinlay, R. E. Morris, K. D. Demadis and A. Cabeza, *Dalton Trans.*, 2012, **41**, 4045–4051.
46 K. D. Demadis, C. Mantzaridis, R. G. Raptis and G. Mezei, *Inorg. Chem.*, 2005, **44**, 4469–4471.
47 K. D. Demadis and N. Stavgianoudaki, in *Metal Phosphonate Chemistry: From Synthesis to Applications*, ed. A. Clearfield and K. D. Demadis, Royal Society of Chemistry, Cambridge, U.K., 2012, ch. 14, pp. 438–492.
48 M. Taddei, F. Costantino, A. Ienco, A. Comotti, P. V. Dau and S. M. Cohen, *Chem. Commun.*, 2013, **49**, 1315–1317.
49 R. F. Mendes, D. Ananias, L. D. Carlos, J. Rocha and F. A. Almeida Paz, *Cryst. Growth Des.*, 2017, **17**, 5191–5199.
50 A. D. G. Firmino, F. Figueira, J. P. C. Tomé, F. A. Almeida Paz and J. Rocha, *Coord. Chem. Rev.*, 2018, **355**, 133–149.
51 *APEX2 v2014.9-0*, Bruker AXS Inc., Madison, WI, 2014.
52 A. Boultif and D. Louër, *J. Appl. Crystallogr.*, 2004, **37**, 724–731.
53 H. M. Rietveld, *J. Appl. Crystallogr.*, 1969, **2**, 65–71.
54 A. C. Larson and R. B. Von Dreele, *General Structure Analysis System (GSAS)*, Los Alamos National Laboratory Report LAUR, 2004, pp. 86–748.
55 *winDETA*, Novocontrol GmbH, Hundsangen, Germany, 1995.
56 D. Massiot, F. Fayon, M. Capron, I. King, S. Le Calvé, B. Alonso, J.-O. Durand, B. Bujoli, Z. Gan and G. Hoatson, *Magn. Reson. Chem.*, 2002, **40**, 70–76.
57 A. Moschona, N. Plesu, G. Mezei, A. G. Thomas and K. D. Demadis, *Corros. Sci.*, 2018, DOI: 10.1016/j.corsci.2018.09.021.
58 E. Akyol, M. Öner, E. Barouda and K. D. Demadis, *Cryst. Growth Des.*, 2009, **9**, 5145–5154.
59 M. Bazaga-García, M. Papadaki, R. M. P. Colodrero, P. Olivera-Pastor, E. R. Losilla, B. Nieto-Ortega, M. A. G. Aranda, D. Choquesillo-Lazarte, A. Cabeza and K. D. Demadis, *Chem. Mater.*, 2015, **27**, 424–435.
60 K. D. Demadis, M. Papadaki and I. Cisarova, *ACS Appl. Mater. Interfaces*, 2010, **2**, 1814–1816.
61 R. M. P. Colodrero, A. Cabeza, P. Olivera-Pastor, J. Rius, D. Choquesillo-Lazarte, J. M. García-Ruiz, M. Papadaki, K. D.

Demadis and M. A. G. Aranda, *Cryst. Growth Des.*, 2011, **11**, 1713–1722.
62 K. D. Demadis, M. Papadaki, R. G. Raptis and H. Zhao, *J. Solid State Chem.*, 2008, **181**, 679–683.
63 K. D. Demadis, M. Papadaki, R. G. Raptis and H. Zhao, *Chem. Mater.*, 2008, **20**, 4835–4846.
64 R. M. P. Colodrero, P. Olivera-Pastor, A. Cabeza, M. Papadaki, K. D. Demadis and M. A. G. Aranda, *Inorg. Chem.*, 2010, **49**, 761–768.
65 K. D. Demadis and S. D. Katarachia, *Phosphorus, Sulfur Silicon Relat. Elem.*, 2004, **179**, 627–648.
66 K. D. Demadis, S. D. Katarachia and M. Koutmos, *Inorg. Chem. Commun.*, 2005, **8**, 254–258.
67 K. D. Demadis, S. D. Katarachia, H. Zhao, R. G. Raptis and P. Baran, *Cryst. Growth Des.*, 2006, **6**, 836–838.
68 L. Jiménez-García, A. Kaltbeitzel, V. Enkelmann, J. S. Gutmann, M. Klapper and K. Müllen, *Adv. Funct. Mater.*, 2011, **21**, 2216–2224.
69 P. Colomban, *Proton Conductors: Solids, Membranes and Gels Materials and Devices. Chemistry of Solid State Materials*, Cambridge University Press, Cambridge, U.K., 1992, vol. 2.
70 A. Florencia-Crespi, A. Jesús-Byrne, D. Vega, A. Karina-Chattah, G. A. Monti and J. M. Lázaro-Martínez, *J. Phys. Chem. A*, 2018, **122**, 601–609.
71 R. M. P. Colodrero, K. E. Papathanasiou, N. Stavgianoudaki, P. Olivera-Pastor, E. R. Losilla, M. A. G. Aranda, L. León-Reina, J. Sanz, I. Sobrados, D. Choquesillo-Lazarte, J. M. García-Ruiz, P. Atienzar, F. Rey, K. D. Demadis and A. Cabeza, *Chem. Mater.*, 2012, **24**, 3780–3792.